JOURNAL OF PROPULSION AND POWER
Vol. 16, No. 4, July–August 2000

Thermal State-of-Charge of Space Solar Dynamic Heat Receivers

Carsie A. Hall III*
University of New Orleans, New Orleans, Louisiana 70148
Emmanuel K. Glakpe† and Joseph N. Cannon‡
Howard University, Washington, D.C. 20059
and
Thomas W. Kerslake§
NASA John H. Glenn Research Center at Lewis Field, Cleveland, Ohio 44135

A theoretical framework is developed to determine the so-called thermal state-of-charge in solar heat receivers employing encapsulated phase change materials that undergo cyclic melting and freezing, and results are presented for the solar heat receiver component of NASA John H. Glenn Research Center at Lewis Field's Ground Test Demonstration System. The concepts of available power, virtual source temperature, and minimum gas available power are used as the bases for determining the state-of-charge. The state-of-charge is characterized in the subcooled, two-phase, and superheat regimes as well as startup, transition, and balanced-orbit modes. Baseline conjugate and primary state-of-charge curves are generated based on a priori known baseline system operating conditions through measurable parameters. Results indicate that for the baseline primary state-of-charge curve in balanced-orbit mode, there is a 33% energy margin (from the minimum state-of-charge line) at sunrise that indicates safe operation of the solar dynamic system; at sunset, the primary state-of-charge reaches 76%. Results for parametric changes indicate that the state-of-charge in the sensible regimes is completely reversed in the latent regime.

Nomenclature

A = area
c = specific heat of solid or liquid phase change material (PCM)
c_p = working fluid specific heat at constant pressure
D_{ap} = aperture diameter
D_{cav} = active cavity diameter
F = geometric view factor
h = enthalpy per unit mass
h_{sf} = PCM latent heat of fusion
M = total number of axial nodes along tube or total PCM mass
$\dot{m}$ = working fluid mass flow rate
N = total number of tubes in receiver
P = working fluid pressure
$\dot{Q}$ = heat transfer rate
R = specific gas constant
$\dot{S}_{\mathrm{gen}}$ = entropy generation rate
Ste = modified Stefan number
s, S = specific, total entropy
T = temperature
T_{ap} = effective aperture or virtual source temperature
T_m = PCM melt temperature
T_0 = environmental dead state temperature
t = time
u, U = specific, total internal energy
V = total volume
$\dot{W}$ = rate of work transfer
z = axial location
β_1 = first conjugate state-of-charge (SOC) function
β_2 = second conjugate SOC function
γ = ratio of specific heats
ε = thermal capacitance ratio
ρ = density
σ = Stefan–Boltzmann constant
τ_{cyc} = total orbit period
τ_{off} = eclipse period
τ_{on} = sun period
Φ = primary SOC function
χ_j = jth tube mass fraction

Subscripts

ap = aperture
av = average
in = tube inlet
losses = losses through shell and aperture
max = maximum
min = minimum
out = tube outlet
rcvr = receiver

Introduction

SOLAR heat receivers are very critical components in the production of electric power via solar dynamic power systems (SDPSs). During operation, the SDPS uses 1) a concentrator to collect and focus the incident energy onto the aperture plane of a central receiver; 2) a central receiver to collect and distribute, with minimal losses, the reflected energy from the concentrator; 3) a series of working fluid tubes aligned along the periphery of the receiver to absorb the distributed energy as heat, thus raising the temperature of the working fluid flowing through the tubes; 4) a turbine to expand the high-temperature working fluid to produce mechanical work via a rotating shaft; 5) a compressor to circulate the working fluid through the working fluid tubes; 6) an alternator to convert mechanical shaft motion into electric power; and 7) a heat rejection system to reject the remaining cycle waste heat. A recuperator is often added to increase the thermal efficiency of the thermodynamic cycle (typically a closed Brayton cycle as shown in Fig. 1).

Received 22 January 1999; revision received 13 July 1999; accepted for publication 20 July 1999.

*Assistant Professor, Department of Mechanical Engineering; cahall@uno.edu. Member AIAA.

†Professor, College of Engineering, Architecture and Computer Sciences. Member AIAA.

‡Professor, College of Engineering, Architecture and Computer Sciences.

§Power Systems Engineer, Power and Propulsion Office, Analysis and Management Branch.

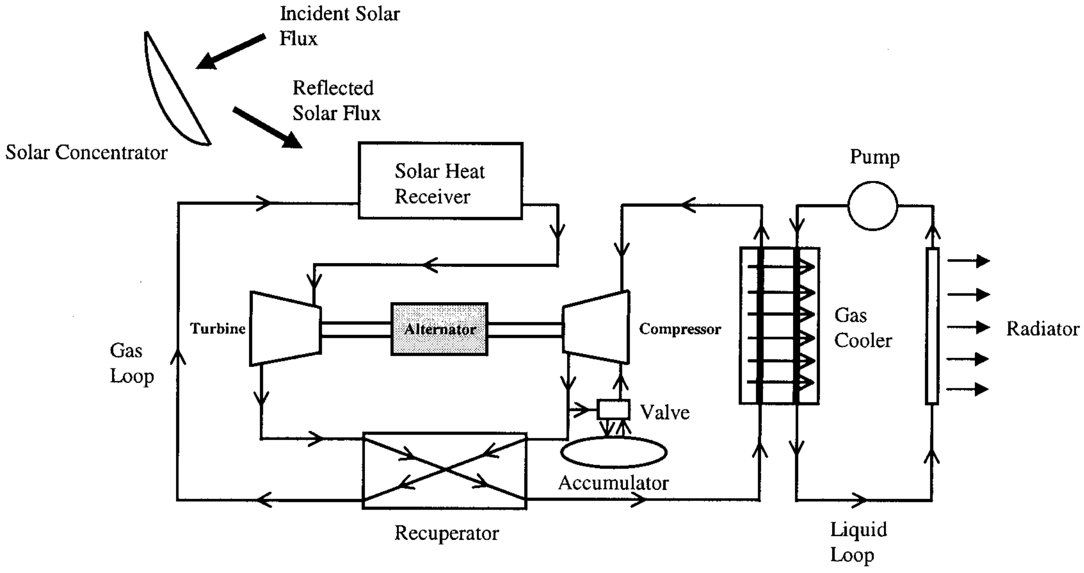

Fig. 1 Thermodynamic cycle for closed Brayton engine integrated with solar heat receiver.

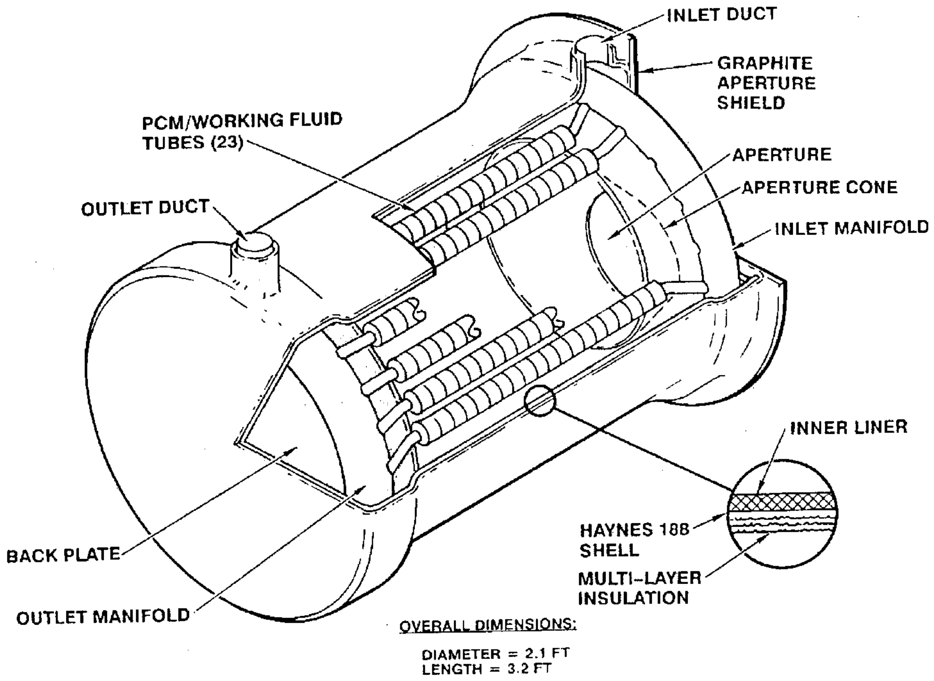

Fig. 2 Solar heat receiver design (provided courtesy of AlliedSignal Aerospace).

Solar heat receivers employing encapsulated phase change materials (PCMs) have the advantage over sensible heat receivers of requiring less mass while producing higher energy storage densities. This, in turn, makes them ideal candidates for energy storage in the space environment where temperatures are sufficiently high, and PCMs with high latent heats of fusion become indispensable.

The instantaneous amount of PCM in the liquid phase (melt fraction) was identified by Strumpf et al.[1] as an indicator of the state-of-charge (SOC). However, it has been recognized that the melt fraction is a better indicator of PCM effectiveness or some performance measure, for example, efficiency, of the receiver as it relates to incorporating phase change storage. According to NASA,[2] "Techniques are needed to determine the so-called receiver state-of-charge, or the quantity of stored thermal energy within the receiver." However, this idea can be extended on second-law grounds because energy quality can be considered a factor in determining the true SOC.

In this paper, a theoretical framework on the thermal SOC of solar heat receivers employing latent heat thermal energy storage is developed. It will be shown that the available energy stored in the receiver is related to a newly defined, time-dependent SOC function that may be completely characterized by measurable parameters. Knowledge of the SOC allows for better control strategies relating to power management schemes during such operations as peak power demand and emergency shutdowns with subsequent restarts. It also helps to better identify the energy startup characteristics of the solar heat receiver in relation to the entire solar dynamic (SD) system, which ensures safe operation of the SD system through all modes and regimes of operation.

Theoretical Framework

Solar Heat Receiver Available Power

The available power of any device is the maximum rate at which energy may be extracted by a work transfer interaction if the device is allowed to come into total (thermal, mechanical, and chemical) equilibrium with its surroundings at some dead state.[3] Shown in Fig. 2

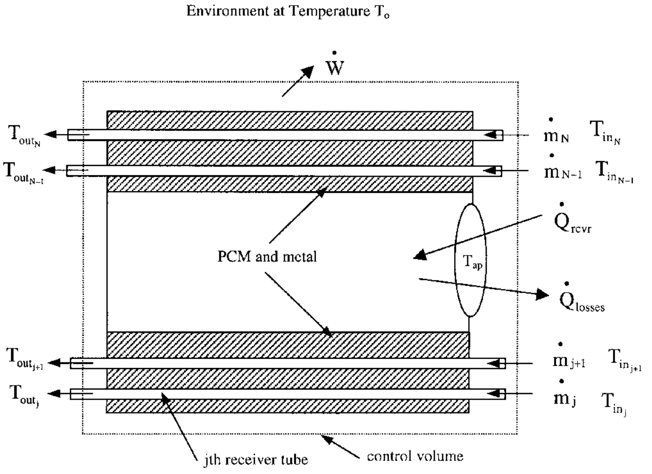

Fig. 3 Solar heat receiver available power and SOC model indicating control volume.

is a typical solar heat receiver design, and Fig. 3 is the model (including control volume) used to derive an expression for the available energy stored in the receiver. An energy balance on the entire receiver with a single fluid stream results in the following:

$$\dot W = (\dot m h)_{\mathrm{in}} - (\dot m h)_{\mathrm{out}} + \dot Q_{\mathrm{rcvr}} - \dot Q_{\mathrm{losses}} - \frac{\partial U}{\partial t} \tag{1}$$

where $\dot W$ is the rate of work transfer across the boundary of the control volume (this is what could be theoretically extracted if the receiver was connected to a work-extracting mechanism), h is the enthalpy per unit mass of the working fluid, $\dot Q_{\mathrm{rcvr}}$ is the rate at which energy crosses the aperture plane, $\dot Q_{\mathrm{losses}}$ is the rate at which energy leaves the receiver due to reradiation from the canister surfaces back out through the aperture and conduction losses through the receiver shell, and U is the total internal energy of the receiver. An associated single fluid stream entropy balance results in

$$\frac{\partial S}{\partial t} = (\dot m s)_{\mathrm{in}} - (\dot m s)_{\mathrm{out}} + \frac{\dot Q_{\mathrm{rcvr}}}{T_{\mathrm{ap}}} - \frac{\dot Q_{\mathrm{losses}}}{T_0} + \dot S_{\mathrm{gen}} \tag{2}$$

where T_{ap} is defined in the next section and $\dot S_{\mathrm{gen}}$ is the rate of entropy generation inside the receiver. Subsequently eliminating the power loss term between Eqs. (1) and (2) gives

$$\dot W = [\dot m(h - T_0 s)]_{\mathrm{in}} - [\dot m(h - T_0 s)]_{\mathrm{out}} + \dot Q_{\mathrm{rcvr}}\left(1 - \frac{T_0}{T^*}\right) - T_0 \dot S_{\mathrm{gen}} - \frac{\partial}{\partial t}(U - T_0 S) \tag{3}$$

in which the maximum is

$$\dot W_{\mathrm{max}} = [\dot m(h - T_0 s)]_{\mathrm{in}} - [\dot m(h - T_0 s)]_{\mathrm{out}} + \dot Q_{\mathrm{rcvr}}\left(1 - \frac{T_0}{T^*}\right) - \frac{\partial}{\partial t}(U - T_0 S) \tag{4}$$

because $\dot S_{\mathrm{gen}} = 0$ for a receiver operating reversibly. Now, it is assumed that the specific enthalpy in Eq. (4) is a function of temperature and pressure whereas the specific entropy is a function of specific enthalpy and pressure. For differential changes in specific enthalpy and specific entropy and through the use of Maxwell's relations, ideal gas assumptions for the working fluid, and the definition of specific heat at constant pressure, it can be shown that, when integrated from inlet conditions to outlet conditions,[3] the available power of an N-tube solar heat receiver (see Fig. 2) can be written as

$$\dot W_{\mathrm{max}} = -\left\{\sum_{j=i}^{N} \dot m_j c_p \left[(T_{\mathrm{out}} - T_{\mathrm{in}})_j - T_0 \ln\left(\frac{T_{\mathrm{out}}}{T_{\mathrm{in}}}\right)_j + T_0\left(\frac{\gamma - 1}{\gamma}\right)\ln\left(\frac{P_{\mathrm{out}}}{P_{\mathrm{in}}}\right)_j\right]\right\} + \dot Q_{\mathrm{rcvr}}\left(1 - \frac{T_0}{T^*}\right) - \frac{\partial}{\partial t}(U - T_0 S) \tag{5}$$

where on defining the jth tube mass fraction as

$$\chi_j = \frac{\dot m_j}{\sum_{i=1}^{N} \dot m_i} \quad \text{such that} \quad \dot m = \sum_{i=1}^{N} \dot m_i \quad \text{and} \quad \sum_{j=1}^{N} \chi_j = 1 \tag{6}$$

Equation (5) can also be expressed in nondimensional form as

$$\frac{\dot W_{\mathrm{max}}}{\dot m c_p T_0} = -\left\{\sum_{j=i}^{N} \chi_j \left[\left(\frac{T_{\mathrm{out}}}{T_0} - \frac{T_{\mathrm{in}}}{T_0}\right)_j - \ln\left(\frac{T_{\mathrm{out}}}{T_{\mathrm{in}}}\right)_j + \left(\frac{\gamma - 1}{\gamma}\right)\ln\left(\frac{P_{\mathrm{out}}}{P_{\mathrm{in}}}\right)_j\right]\right\} + \frac{\dot Q_{\mathrm{rcvr}}}{\dot m c_p T_0}\left(1 - \frac{T_0}{T^*}\right) - \frac{1}{\dot m c_p T_0}\frac{\partial}{\partial t}(U - T_0 S) \tag{7}$$

The internal energy U and entropy S are given, respectively, by

$$U = \sum_{j=1}^{N}\sum_{i=1}^{4} \iiint_{V_{ij}} (\rho u)_{ij}\, \mathrm{d}V_{ij} \tag{8}$$

and

$$S = \sum_{j=1}^{N}\sum_{i=1}^{4} \iiint_{V_{ij}} (\rho s)_{ij}\, \mathrm{d}V_{ij} \tag{9}$$

in which the integration takes place over the ith region and jth tube. On further defining the dimensionless parameters

$$\dot Q^*_{\mathrm{rcvr}} = \frac{\dot Q_{\mathrm{rcvr}}}{(T_0/T_m)(h_{\mathrm{sf}} M/\tau_{\mathrm{cyc}})}, \qquad U^* = \frac{U}{(T_0/T_m)h_{\mathrm{sf}} M}$$
$$S^* = \frac{S}{(h_{\mathrm{sf}}/T_m)M}, \qquad t^* = \frac{t}{\tau_{\mathrm{cyc}}}$$
$$T^*_{\mathrm{out}} = \frac{T_{\mathrm{out}}}{T_0}, \qquad T^*_{\mathrm{in}} = \frac{T_{\mathrm{in}}}{T_0}, \qquad T^*_{\mathrm{ap}} = \frac{T_{\mathrm{ap}}}{T_0} \tag{10}$$

where $\tau_{\mathrm{cyc}} = \tau_{\mathrm{on}} + \tau_{\mathrm{off}}$, the following dimensionless receiver available power results:

$$\frac{\dot W_{\mathrm{max}}}{\dot m c_p T_0} = -\left\{\sum_{j=i}^{N} \chi_j \left[\left(T^*_{\mathrm{out}} - T^*_{\mathrm{in}}\right)_j - \ln\left(\frac{T^*_{\mathrm{out}}}{T^*_{\mathrm{in}}}\right)_j + \left(\frac{\gamma - 1}{\gamma}\right)\ln\left(\frac{P_{\mathrm{out}}}{P_{\mathrm{in}}}\right)_j\right]\right\} + \left(\frac{\varepsilon}{Ste}\right)\dot Q^*_{\mathrm{rcvr}}\left(1 - \frac{1}{T^*_{\mathrm{ap}}}\right) - \frac{\partial}{\partial t^*}(U^* - S^*) \tag{11}$$

where $Ste = cT_m/h_{\mathrm{sf}}$ is the modified Stefan number and $\varepsilon = Mc/\dot m \tau_{\mathrm{cyc}} c_p$ is the thermal capacitance ratio expressing the relative amounts of sensible heat capacity of the PCM to sensible heat capacity of the working fluid. In addition, the dimensionless available power equation can be interpreted physically as follows: The first bracketed term is the available power loss from the receiver to the gas, the second term is the available power gain by the receiver due to the net heat interaction across the aperture plane, and the last term is the available power loss or gain due to unsteady charging and discharging. Furthermore, an interesting comparison can be made between the fraction of incident power available at the aperture plane, expressed in Eq. (11) as

$$\psi = 1 - \left(T_0/T^*\right) = 1 - (1/T^{**}) \tag{12}$$

and that which is reported by Moynihan,[4] that is,

$$\psi' = 1 - \tfrac{4}{3}\left(T_0/T^*\right) + \tfrac{1}{3}\left(T_0/T^*\right)^4 = 1 - \tfrac{4}{3}(1/T^{**}) + \tfrac{1}{3}(1/T^{**})^4 \tag{13}$$

Note that over the anticipated region of operation ($0.1 \leq T_0/T^* \leq 0.3$) the agreement is good.[5]

Virtual Source Temperature

The effective temperature of the aperture due to the net heat interaction across the aperture plane is defined as the virtual source temperature. It expresses continuity of energy reradiated from the outer surfaces of the canisters to the aperture. Therefore, an energy balance on the aperture plane of the receiver shown in Fig. 2 results in

$$\sum_{j=1}^{M+1} A_j F_{j-\mathrm{ap}} \sigma\left[T_j^4(t) - T_{\mathrm{ap}}^4(t)\right] = A_{\mathrm{ap}} F_{\mathrm{ap}-0} \sigma\left[T_{\mathrm{ap}}^4(t) - T_0^4\right] \tag{14}$$

where on solving for the virtual source temperature T_{ap} gives

$$T_{\mathrm{ap}}(t) = \left\{\frac{A_{\mathrm{ap}} F_{\mathrm{ap}-0} \sigma T_0^4 + \sum_{j=1}^{M+1} A_j F_{j-\mathrm{ap}} \sigma T_j^4(t)}{A_{\mathrm{ap}} F_{\mathrm{ap}-0} \sigma + \sum_{j=1}^{M+1} A_j F_{j-\mathrm{ap}} \sigma}\right\}^{\frac{1}{4}} \tag{15}$$

which in dimensionless form is written as

$$T_{\mathrm{ap}}^*(t^*) = \frac{T_{\mathrm{ap}}(t^*)}{T_0}$$

$$= \left\{\frac{1 + \sum_{j=1}^{M+1} (A_j/A_{\mathrm{ap}})(F_{j-\mathrm{ap}}/F_{\mathrm{ap}-0}) T_j^{*4}(t^*)}{1 + \sum_{j=1}^{M+1} (A_j/A_{\mathrm{ap}})(F_{j-\mathrm{ap}}/F_{\mathrm{ap}-0})}\right\}^{\frac{1}{4}} \tag{16}$$

In Eq. (16), the jth area ratio (A_j/A_{ap}) can be written as

$$\frac{A_j}{A_{\mathrm{ap}}} = \frac{\pi D_{\mathrm{cav}} \Delta z}{(\pi/4) D_{\mathrm{ap}}^2} = 4\left(\frac{D_{\mathrm{cav}}}{D_{\mathrm{ap}}}\right)\left(\frac{\Delta z}{D_{\mathrm{ap}}}\right) \tag{17}$$

Notice that Eq. (17) contains one of the cavity aspect ratios ($D_{\mathrm{cav}}/D_{\mathrm{ap}}$) that is a key parameter that affects the thermal performance of the solar heat receiver. Also, the geometric view factors in Eqs. (14–16) are given by analytic expressions found by Howell.[6]

Gas Available Power

Recall the expression given by Eq. (5), which is the instantaneous available energy stored in the receiver. Note that the first term in brackets in Eq. (5) represents the instantaneous available power of the gas before mixing in the outlet manifold. This power, which is the difference between the enthalpy transferred to gas and a term proportional to the entropy transferred to the gas, is rewritten as

$$\dot{W}_{\mathrm{gas}} = \sum_{j=1}^{N} \dot{m}_j c_p \left[(T_{\mathrm{out}} - T_{\mathrm{in}})_j - T_0 \ln\left(\frac{T_{\mathrm{out}}}{T_{\mathrm{in}}}\right)_j + T_0\left(\frac{\gamma - 1}{\gamma}\right) \ln\left(\frac{P_{\mathrm{out}}}{P_{\mathrm{in}}}\right)_j\right] \tag{18}$$

which is expressed in dimensionless form as

$$\frac{\dot{W}_{\mathrm{gas}}}{\dot{m} c_p T_0} = \sum_{j=1}^{N} \chi_j \left\{\left(T_{\mathrm{out}}^* - T_{\mathrm{in}}^*\right)_j - \ln\left(\frac{T_{\mathrm{out}}^*}{T_{\mathrm{in}}^*}\right)_j + \left(\frac{\gamma - 1}{\gamma}\right) \ln\left(\frac{P_{\mathrm{out}}}{P_{\mathrm{in}}}\right)_j\right\} \tag{19}$$

Physically, the reduction in available power associated with the transport of entropy to the gas can be attributed to two sources: 1) heat transfer to the gas across finite temperature differences and 2) frictional effects leading to reductions in pressure along the lengths of each of the tubes in the receiver. The concept of entropy is associated with the amount of unavailable energy within a system. Therefore, the available power of the gas, expressed by Eq. (19), is that which is delivered to the outlet manifold before any mixing takes place. Any further reduction in available power takes place in the outlet manifold due to irreversible mixing of each of the individual fluid streams. Finally, it is observed that all of the parameters in Eq. (19) can either be readily calculated or directly measured.

Mixing-Based Lost Available Power

It is known that the lost available power associated with the gas is proportional to the entropy generation rate, where the proportionality constant is the dead state temperature.[3,7] Expressed mathematically,

$$\dot{W}_{\mathrm{lost}} = T_0 \dot{S}_{\mathrm{gen}} \tag{20}$$

For a solar heat receiver with N tubes and N associated fluid streams, the entropy generation rate due to irreversible fluid stream mixing in the outlet manifold is given by

$$\dot{S}_{\mathrm{gen}} = \dot{m} s_{N+1} - \sum_{j=1}^{N} \dot{m} \chi_j s_j \tag{21}$$

which can be subsequently written in terms of temperatures as

$$\dot{S}_{\mathrm{gen}} = \dot{m} c_p \sum_{j=1}^{N} \chi_j \ln\left(\frac{T_{N+1}}{T_j}\right) \tag{22}$$

where T_j is the fluid outlet temperature of the jth tube just before entering the outlet manifold and $N + 1$ corresponds to mixed mean properties in the outlet manifold just before entering the turbine.[8,9] The corresponding loss in available power from the gas is expressed as

$$\dot{W}_{\mathrm{lost}} = \dot{m} c_p T_0 \sum_{j=1}^{N} \chi_j \ln\left(\frac{T_{N+1}}{T_j}\right) \tag{23}$$

which can be further written in the following nondimensional form:

$$\frac{\dot{W}_{\mathrm{lost}}}{\dot{m} c_p T_0} = \sum_{j=1}^{N} \chi_j \ln\left(\frac{T_{N+1}}{T_j}\right) \tag{24}$$

As expected, when each tube in the receiver is imparted with the same incident flux, the temperature of each gas stream exiting all of the tubes is the same, resulting in no loss in available power. This is revealed in Eq. (24).

Relation Between SOC and Available Power

A dimensionless conjugate SOC function β_1 is defined as the ratio of instantaneous available power stored in the receiver with no available power lost to the working fluid to minimum gas available power required to operate the turbine, or

$$\beta_1 = \frac{\dot{W}^*_{\max}}{\dot{W}_{\min}} = \left(\frac{\varepsilon}{Ste}\right)\left\{\dot{Q}^*_{\mathrm{rcvr}}\left(1 - \frac{1}{T^*_{\mathrm{ap}}}\right) - \frac{\partial}{\partial t^*}(U^* - S^*)\right\}\Bigg/ \sum_{j=1}^{N}\chi_j\left\{\left(T^*_{\min} - T^*_{\mathrm{in}}\right)_j - \ln\left(\frac{T^*_{\min}}{T^*_{\mathrm{in}}}\right)_j + \left(\frac{\gamma - 1}{\gamma}\right)\ln\left(\frac{P_{\min}}{P_{\mathrm{in}}}\right)_j\right\} \tag{25}$$

A second dimensionless conjugate SOC function β_2 is defined as the ratio of instantaneous gas available power to minimum gas available power required to operate the turbine, that is,

$$\beta_2 = \frac{\dot{W}_{\mathrm{gas}}}{\dot{W}_{\min}} = \sum_{j=1}^{N}\chi_j\left\{\left(T^*_{\mathrm{out}} - T^*_{\mathrm{in}}\right)_j - \ln\left(\frac{T^*_{\mathrm{out}}}{T^*_{\mathrm{in}}}\right)_j + \left(\frac{\gamma - 1}{\gamma}\right)\ln\left(\frac{P_{\mathrm{out}}}{P_{\mathrm{in}}}\right)_j\right\}\Bigg/ \sum_{j=1}^{N}\chi_j\left\{\left(T^*_{\min} - T^*_{\mathrm{in}}\right)_j - \ln\left(\frac{T^*_{\min}}{T^*_{\mathrm{in}}}\right)_j + \left(\frac{\gamma - 1}{\gamma}\right)\ln\left(\frac{P_{\min}}{P_{\mathrm{in}}}\right)_j\right\} \tag{26}$$

where the outlet manifold mixing losses have been neglected in both conjugate functions for convenience. On further defining the denominator of Eqs. (25) and (26) as

$$\beta_{\min} = \sum_{j=1}^{N}\chi_j\left\{\left(T^*_{\min} - T^*_{\mathrm{in}}\right)_j - \ln\left(\frac{T^*_{\min}}{T^*_{\mathrm{in}}}\right)_j + \left(\frac{\gamma - 1}{\gamma}\right)\ln\left(\frac{P_{\min}}{P_{\mathrm{in}}}\right)_j\right\} \tag{27}$$

the conjugate SOC functions and $\beta_{\min}$ can be related to the dimensionless receiver available power [Eq. (11)] as

$$\beta_{\min}(\beta_1 - \beta_2) = \dot{W}_{\max}/\dot{m}c_p T_0 \tag{28}$$

Now, a primary SOC function can be defined as the dimensionless combination

$$\Phi \equiv \frac{\beta_1 - 1}{\beta_{\max} - 1} \tag{29}$$

such that Φ is always in the range $0 \le \Phi \le 1$. Notice that $\beta_{\min}$ is β_2 evaluated at $T_{\mathrm{out}} = T_{\min}$ and that $P_{\mathrm{out}} = P_{\min}$ and $\beta_{\max}$ is the maximum value that the first conjugate SOC function β_1 can take on, which can be shown to be

$$\beta_{\max} = \frac{\dot{W}^*_{\max}\big|_{\mathrm{ss}}}{\dot{W}^*_{\min}} = \left(\frac{\varepsilon}{Ste}\right)\left\{\dot{Q}^*_{\mathrm{rcvr}}\left(1 - \frac{1}{T^*_{\mathrm{ap(ss)}}}\right)\right\}\Bigg/ \sum_{j=1}^{N}\chi_j\left\{\left(T^*_{\min} - T^*_{\mathrm{in}}\right)_j - \ln\left(\frac{T^*_{\min}}{T^*_{\mathrm{in}}}\right)_j + \left(\frac{\gamma - 1}{\gamma}\right)\ln\left(\frac{P_{\min}}{P_{\mathrm{in}}}\right)_j\right\} \tag{30}$$

which is just the steady-state equivalent of Eq. (25). Therefore, the maximum SOC is achieved when the thermodynamic state of the receiver is driven to steady-state conditions even though the system is designed to operate under cyclic conditions.

The unsteady term in the numerator of the first conjugate SOC function can be expressed entirely in terms of the time derivative of the internal energy by recalling that for pure substances that undergo reversible changes in state, the first law is written as

$$\mathrm{d}U = T\,\mathrm{d}S - P\,\mathrm{d}V \tag{31}$$

which on a rate basis is

$$\frac{\mathrm{d}U}{\mathrm{d}t} = T\frac{\mathrm{d}S}{\mathrm{d}t} - P\frac{\mathrm{d}V}{\mathrm{d}t} \tag{32}$$

Solving Eq. (32) for the time derivative of entropy yields

$$\frac{\mathrm{d}S}{\mathrm{d}t} = \frac{1}{T}\left(\frac{\mathrm{d}U}{\mathrm{d}t} + P\frac{\mathrm{d}V}{\mathrm{d}t}\right) \tag{33}$$

A further reduction can be achieved by neglecting the last term in Eq. (33) involving the time derivative of volume. This is unquestionably a reasonable assumption for the canister and working fluid tube regions, even though small changes do occur due to thermal expansions and contractions since the receiver is operated in a cyclic manner. However, the PCM region requires a little more insight. It is certainly consistent with the assumption of no void or even a stationary void to neglect $\mathrm{d}V/\mathrm{d}t$ in the PCM region. It is also reasonable to assume that even when a void is forming, the low vapor pressure of the void filled with PCM vapor contributes negligibly to $p\,\mathrm{d}V/\mathrm{d}t$, which is essentially the rate of work done due to expansion and/or contraction of the liquid PCM region. Moreover, in the doughnut region, the total volume remains constant even though the phases are redistributed during phase change, including void formation. Furthermore, solid/liquid and liquid/void interface curvatures are expected to have negligibly small effects on the $p\,\mathrm{d}V/\mathrm{d}t$ term. As a result, Eq. (33) becomes

$$\frac{\mathrm{d}S}{\mathrm{d}t} = \frac{1}{T}\frac{\mathrm{d}U}{\mathrm{d}t} \tag{34}$$

Now, the dimensional form of the unsteady term in the expression for the available power of the receiver [in Eq. (3)] can be written as

$$\frac{\partial}{\partial t}(U - T_0 S) = \left(1 - \frac{T_0}{T}\right)\frac{\partial U}{\partial t} \tag{35}$$

The advantage of eliminating the entropy rate term in favor of the internal energy rate term is that the internal energy rate term can be calculated (or measured) in terms of measurable parameters. Furthermore, the dimensionless form of Eq. (35) is

$$\left(\frac{1}{\dot{m}c_p T_0}\right)\frac{\partial}{\partial t}(U - T_0 S) = \left(\frac{\varepsilon}{Ste}\right)\left(1 - \frac{1}{T^*_{\mathrm{eff}}}\right)\frac{\mathrm{d}U^*}{\mathrm{d}t^*} \tag{36}$$

and the dimensionless effective cavity temperature is defined in the usual manner:

$$T^*_{\mathrm{eff}} = T_{\mathrm{eff}}/T_0 \tag{37}$$

in which T_{eff} is the mean tube surface temperature. Moreover, the integral of the unsteady term over an entire balanced orbit vanishes. That is, from end of the ith cycle to the beginning of the $(i + 1)$st cycle, it is required that

$$\int_{\tau_{\mathrm{cyc}_i}}^{\tau_{\mathrm{cyc}_{i+1}}}\left(1 - \frac{T_0}{T_{\mathrm{eff}}}\right)\left(\frac{\mathrm{d}U}{\mathrm{d}t}\right)\mathrm{d}t = 0 \tag{38}$$

which can also be used to evaluate the way in which the effective cavity temperature is calculated. Of course, under steady-state conditions, the integrand of Eq. (38) vanishes automatically.

In lieu of Eq. (36), the dimensionless available power of the receiver expressed by Eq. (11) can be rewritten in the form

$$\frac{\dot{W}_{\max}}{\dot{m} c_p T_0} = -\left\{\sum_{j=1}^{N} \chi_j \left[\left(T^*_{\mathrm{out}} - T^*_{\mathrm{in}}\right)_j - \ln\left(\frac{T^*_{\mathrm{out}}}{T^*_{\mathrm{in}}}\right)_j + \left(\frac{\gamma - 1}{\gamma}\right)\ln\left(\frac{P_{\mathrm{out}}}{P_{\mathrm{in}}}\right)_j\right]\right\} + \left(\frac{\varepsilon}{Ste}\right)\left\{\dot{Q}^*_{\mathrm{rcvr}}\left(1 - \frac{1}{T^*_{\mathrm{ap}}}\right) - \left(1 - \frac{1}{T^*_{\mathrm{eff}}}\right)\frac{\mathrm{d}U^*}{\mathrm{d}t}\right\} \tag{39}$$

which subsequently implies that the first conjugate SOC function is given by

$$\beta_1 = \frac{\dot{W}^*_{\max}}{\dot{W}^*_{\min}} = \left(\frac{\varepsilon}{Ste}\right)\left\{\dot{Q}^*_{\mathrm{rcvr}}\left(1 - \frac{1}{T^*_{\mathrm{ap}}}\right) - \left(1 - \frac{1}{T^*_{\mathrm{eff}}}\right)\frac{\mathrm{d}U^*}{\mathrm{d}t^*}\right\} \Bigg/ \sum_{j=1}^{N} \chi_j \left\{\left(T^*_{\min} - T^*_{\mathrm{in}}\right)_j - \ln\left(\frac{T^*_{\min}}{T^*_{\mathrm{in}}}\right)_j + \left(\frac{\gamma - 1}{\gamma}\right)\ln\left(\frac{P_{\min}}{P_{\mathrm{in}}}\right)_j\right\} \tag{40}$$

where the unsteady term $(\mathrm{d}U^*/\mathrm{d}t^*)$ is inferred from the difference between the total solar power crossing the aperture plane and the total reradiated power from the receiver surfaces to the surrounding environment. More details on the formulation can be found in Ref. 10.

It should also be pointed out the unsteady term in Eq. (40) can be implicitly calculated through knowledge of the PCM melt rate. In the present paper, the PCM melt fraction and PCM melt rate is calculated using the enthalpy method of Shamsundar and Sparrow,[11] which eliminates the need for explicit solid-liquid interface tracking.

Modes of SOC Characterization

The operation of SD power systems can be categorized according to their operating modes. These modes of operation include 1) startup, 2) transition, 3) balanced orbit, 4) steady state, and 5) shutdown (including restart). Each of these modes possesses unique qualitative behavior with respect to their thermal performance characteristics and SOC characterization.

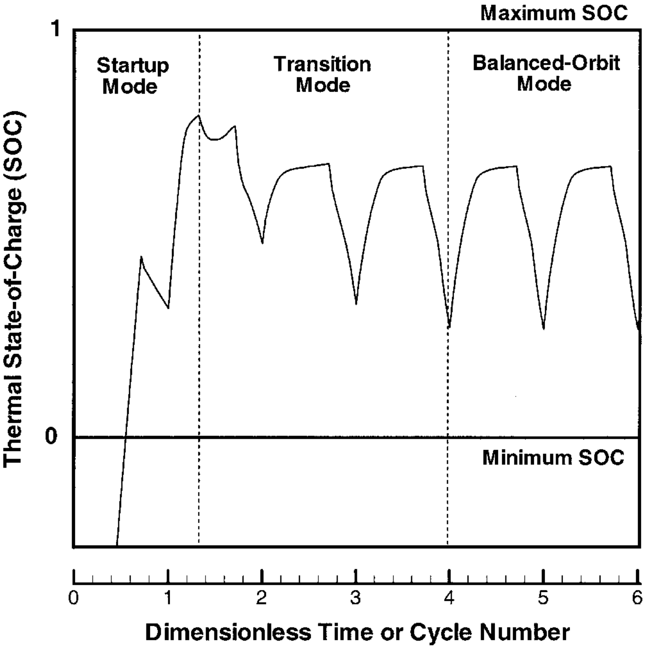

Fig. 4 Qualitative illustration of startup, transition, and balanced-orbit modes of SOC characterization.

Shown in Fig. 4 is a qualitative rendering of the first three of the aforementioned operating modes. The region indicated by startup mode characterizes the initial heating phase of the SD system whereby the receiver is heated up (or charged) with virtually no gas flow until a predetermined temperature setpoint is reached. After this setpoint is reached, the turboalternator-compressor (TAC) is started with an external power source that starts up the mass flow of the gas through the receiver. During this mode, indicated by transition mode (Fig. 4), incremental increases in TAC speed are made until a predetermined operating TAC speed is reached. The end of the transition mode is followed by a balanced-orbit mode, whereby system performance parameters are repeated from one sunrise to the next and from one sunset to the next. In relation to the other operating modes, the characterization of the balanced-orbit mode is more important because the response of the SD system to changes in orbital conditions or off-design conditions can be more easily assessed or even predicted. In addition, the characterization of the balanced-orbit mode subsequently leads to knowledge of long-term energy balance or maintenance requirements.

Results and Discussion

Baseline Curve for Conjugate SOC Parameters

The baseline operating conditions of the NASA John H. Glenn Research Center at Lewis Field Ground Test Demonstration (GTD) Solar Dynamic (SD) Power system are taken from experimental data reported by Mason[8] and Shaltens and Mason.[9] Under normal balanced-orbit operation, these conditions are in the following ranges: receiver heat input, 12.6 kW; TAC operating speed, 48,000–56,000 rpm; average receiver inlet temperature, 1408–1608°R (782–838 K); and sink temperature, 360–375°R (200–208 K).

Note that throughout the results presented in this and later sections, the dimensionless receiver heat input given by Eq. (10) is fixed at $\dot{Q}^*_{\mathrm{rcvr}} = 10.27$, corresponding to $\dot{Q}_{\mathrm{rcvr}} = 12.6$ kW, $T_0 = 375$°R (208 K), and $\tau_{\mathrm{cyc}} = 93$ min. The baseline TAC speed is 52,000 rpm, which corresponds to a working fluid mass flow rate of $\dot{m} = 0.3333$ lb m/s (152 g/s) and $\varepsilon/Ste = 0.0875$. The modified Stefan number is fixed at $Ste = 2.6$, which would seem to indicate a predominance of PCM sensible heat over PCM latent heat. However, in this paper, the modified Stefan number is defined with respect to the absolute PCM melt temperature rather than a characteristic temperature difference. Therefore, caution should be used with regard to its physical interpretation. Furthermore, the baseline dimensionless minimum gas available power is fixed at $\dot{W}^*_{\min} = 0.1861$, which corresponds to a minimum turbine gas inlet temperature of $T_{\min} = 1600$°R (889 K) and an average receiver gas inlet temperature of $T_{\mathrm{in}} = 1508$°R (838 K). The chosen $T_{\min}$ is based on a cycle temperature ratio of four and a compressor inlet temperature of 400°R (222 K). Figure 5 shows the temporal development of the two conjugate SOC parameters and the resulting dimensionless receiver available power from cold startup conditions [532°R (296 K)] to balanced-orbit conditions. The first observation to make is that there are indeed three modes of operation: 1) startup mode, which extends from the first cycle into the second cycle, 2) transition mode, which spans part of the second cycle up to the fifth cycle, and 3) balanced-orbit mode, which is reached on the sixth cycle. During startup mode, the working fluid mass flow rate is kept very low (two orders of magnitude lower than normal) to facilitate faster heatup of the receiver. During this mode (see Fig. 6 for details), the first conjugate SOC parameter β_1 first decreases due to the low fraction of incident power available at the aperture; as heating of the receiver progresses, the surface temperatures become larger, which increases the fraction of incident power available at the aperture and β_1 increases. This phenomenon occurs during the first cycle. During the second cycle, β_1 continues to increase from the previous end-of-cycle (sunrise) value until the working fluid mass flow rate is tripped due to a preset maximum canister surface temperature of 1900°R (1056 K). This marks the beginning of the transition mode, where the system performance parameters (including SOC)

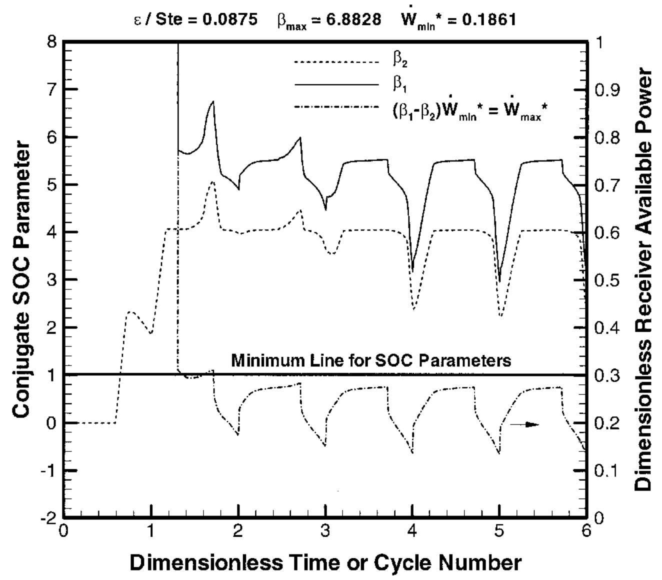

Fig. 5 Variation of baseline conjugate SOC parameters over six orbit cycles.

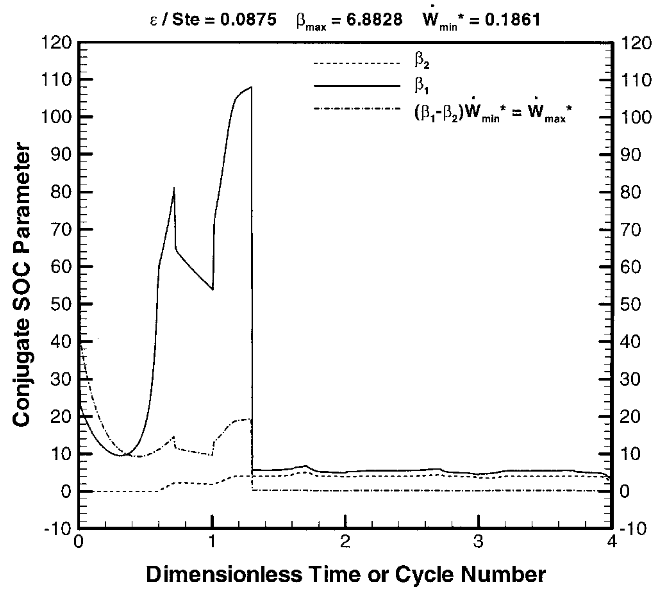

Fig. 6 Variation of baseline conjugate SOC parameters over four orbit cycles with details of the startup and transition modes.

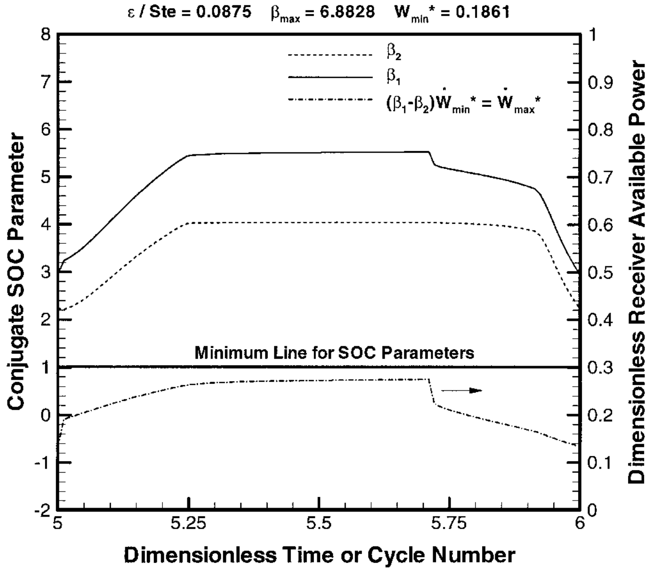

Fig. 7 Variation of baseline conjugate SOC parameters over the balanced-orbit mode.

begin to adjust to the increased working fluid mass flow rate; this adjustment continues into the fifth cycle. It is also observed that β_1 is always above the minimum line corresponding to $\beta_1 = 1$, which is a requirement for normal operation of the SD system. The second conjugate SOC parameter β_2 has different qualitative behavior from that of the first conjugate SOC parameter β_1. During startup mode, the receiver gas exit temperature is fed back as the receiver gas inlet temperature and β_2 remains zero until a preset operating receiver gas inlet temperature of 1508°R (838 K) is reached; this occurs during the first cycle. With the receiver gas inlet temperature now fixed at 1508°R (838 K), the receiver gas exit temperature is cycled in accordance with other parameters in the system; this increases β_2 above the minimum SOC line ($\beta_2 = 1$) during the first cycle. During the second cycle, β_2 increases even on through the trip point, where the working fluid mass flow rate is increased to its normal operating value. This is due to local superheating of the PCM that causes spikes in the receiver gas exit temperature and, thus, the β_2 parameter. As expected, β_2 begins to adjust to the increased working fluid mass flow rate in the transition mode (cycles 2–5). Although quantitatively different, the dimensionless receiver available power is qualitatively similar to the first conjugate SOC parameter β_1. This is due to the predominance of β_1 over β_2 through all of the orbit cycles. It is also observed that the dimensionless receiver available power reaches a balanced-orbit mode faster than the individual conjugate SOC parameters. Moreover, the dimensionless receiver available power is quantitatively smaller than the conjugate SOC parameters, which is a first indication that the receiver available power alone is an insufficient measure of the receiver SOC.

The temporal variation of the baseline conjugate SOC parameters over the balanced-orbit mode (sixth cycle) is shown in Fig. 7. The resulting dimensionless receiver available power is also plotted in Fig. 7. It appears that the behavior of the first conjugate SOC parameter β_1 can be divided into four regions: 1) In the first region (approximately the first 25% of the total orbit cycle), β_1 increases due to sensible heating of the PCM salt. 2) In the second region (approximately the next 50% of the total orbit cycle), β_1 flattens out to a maximum value of about 5.6 due to increased melting of the PCM. 3) In the third region, where the eclipse starts (approximately the next 15% of the total orbit cycle), β_1 first decreases sharply due to transition from sun period to eclipse period, after which it decreases less rapidly due to removal of the PCM latent heat. 4) In the fourth region (approximately the last 10% of the total orbit cycle), β_1 drops back to its sunrise value of about 3 due to continued removal of the salt sensible heat.

The qualitative behavior of the second conjugate SOC parameter β_2 can be divided into three regions: 1) In the first region (approximately the first 25% of the total orbit cycle), β_2 increases due to sensible heating effects in the PCM and working fluid. 2) In the second region (approximately the next 65% of the total orbit cycle), which extends into the eclipse cycle, β_2 flattens out to a maximum value of about 4 due to PCM latent heat effects. 3) In the third region (approximately the remaining 10% of the total orbit cycle), β_2 decreases to its sunrise value of about 2.2 due to sensible heat removal in the PCM salt. Furthermore, the dimensionless receiver available power is shown to be qualitatively similar to the first conjugate SOC parameter β_1, although the slopes in the different regions are not as dramatic. Quantitatively, the dimensionless receiver available power varies between about 0.13 at sunrise to approximately 0.28 at sunset.

Baseline Curve for Primary SOC

Figure 8 shows the temporal development of the baseline primary SOC from cold start conditions up to balanced-orbit mode. It should first be observed that the primary SOC is qualitatively similar to the first conjugate SOC function β_1. This is to be expected because the

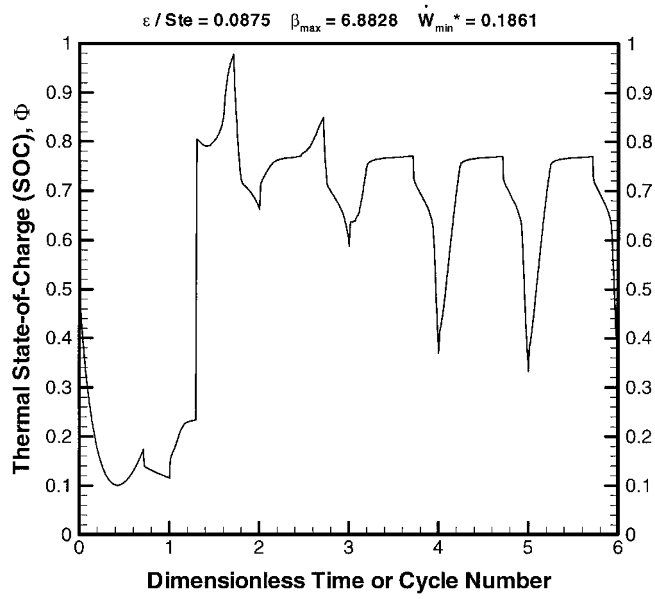

Fig. 8 Variation of baseline primary SOC over six orbit cycles.

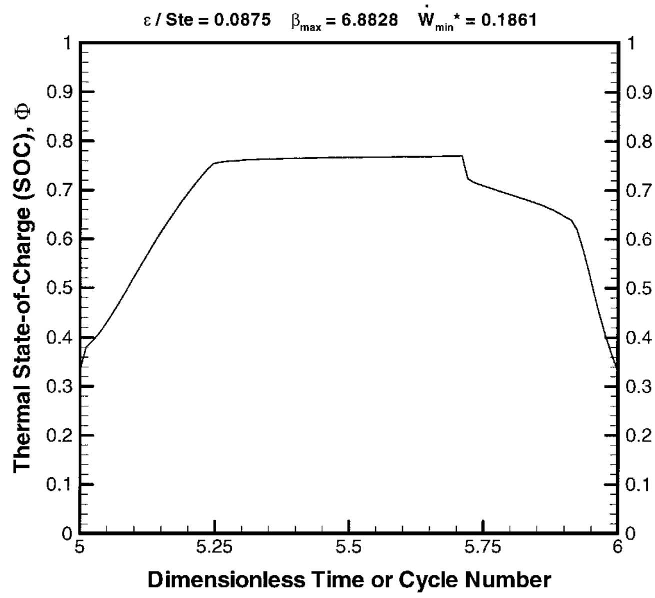

Fig. 9 Variation of baseline primary SOC over the balanced-orbit mode.

primary SOC function is a dimensionless combination of the first conjugate SOC function β_1 as illustrated by Eq. (29); the primary SOC function Φ is scaled so that it varies in the range $0 \leq \Phi \leq 1$. When scaled in this manner, it is convenient to track the SOC with respect to the minimum ($\Phi = 0$) and maximum ($\Phi = 1$) SOC states. Note that the qualitative description of the temporal variation of the baseline first conjugate SOC parameter β_1 can also be used to explain the qualitative behavior of the baseline primary SOC parameter Φ. Whereas Fig. 8 illustrates the temporal variation over the startup and transition modes, Fig. 9 shows the temporal variation over the balanced-orbit mode. Again, the qualitative behavior of the baseline primary SOC parameter Φ over the balanced-orbit mode is similar to the qualitative behavior of the baseline first conjugate SOC parameter β_1. Quantitatively, the baseline primary SOC parameter attains a minimum value of approximately 33% at sunrise and a maximum value of about 76% at sunset.

Another point of interest concerns the equivalent thermal power output corresponding to the baseline conjugate SOC parameters. Therefore, the variation of the equivalent thermal power over the startup, transition, and balanced-orbit modes is given in Fig. 10. The

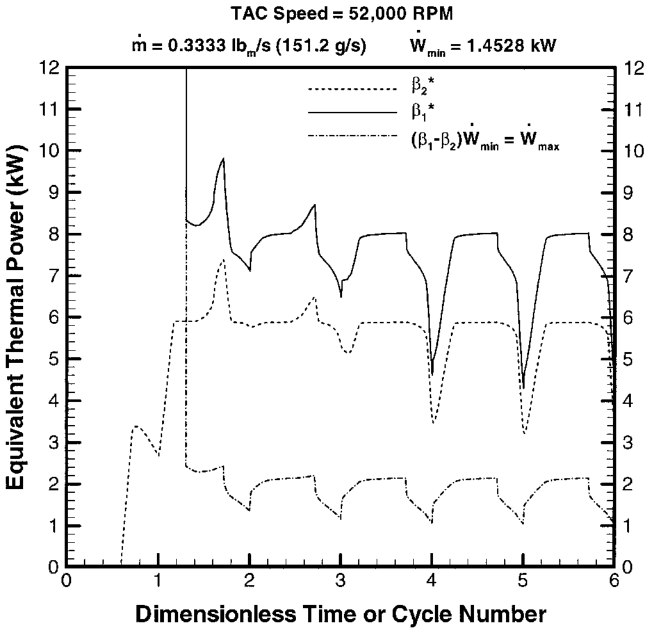

Fig. 10 Variation of equivalent thermal power corresponding to the conjugate SOC parameters over six orbit cycles.

most useful quantities to extract from Fig. 10 are the balanced-orbit sunrise and sunset equivalent thermal powers corresponding to the first and second conjugate SOC parameters. Thus, the approximate equivalent thermal power values corresponding to the first conjugate SOC parameter β_1 are 4.3 and 8 kW at sunrise and sunset, respectively. For the second conjugate SOC parameter β_2 these values are approximately 3.2 and 5.9 kW at sunrise and sunset, respectively. Finally, the receiver available power varies between about 1.1 and 2.2 kW at sunrise and sunset, respectively; these values are clearly insufficient measures of the receiver SOC.

Perturbation Analysis of SOC Curve

In this section, changes in system measurable parameters are made to determine their cumulative effects on the primary SOC function Φ and second conjugate SOC function β_2. In particular, parametric changes in TAC speed (via working fluid mass flow rate) and sun period/total orbit period ratio are examined. These changes are manifested through changes in their dimensionless counterparts. For example, lowering the TAC speed from 52,000 to 48,000 rpm results in a change in thermal capacitance ratio from $\varepsilon/Ste = 0.0875$–0.0933 because the corresponding working fluid mass flow rate changes from 0.3333 lb m/s (152 g/s) to 0.3125 lb m/s (142 g/s). The effect of parametric changes in the thermal capacitance ratio on the primary SOC function over the balanced-orbit mode is shown in Fig. 11. The dimensionless minimum gas available power is fixed at 0.1861. The primary SOC curves that result from changes in the thermal capacitance ratio are superimposed on the baseline primary SOC curve to facilitate comparisons. Several interesting phenomena can be observed in the balanced-orbit mode. First is that, for the higher thermal capacitance ratio (lower TAC speed) of 0.0933, the SOC is higher for most of the initial portion of the sun period. This is to be expected because this initial portion corresponds to sensible heating of the PCM salt, and the lower TAC speed results in lower energy extraction rates (via unsteady available power). The opposite effect is observed for the lower thermal capacitance ratio (higher TAC speed) of 0.0824. In the latent regime, indicated by the flat region of each curve, the aforementioned phenomena is reversed. That is, for all representative TAC speeds in the latent regime, the unsteady available power remains constant; however, the lower TAC speed (higher thermal capacitance ratio) results in a higher unsteady available power level in this regime because the PCM melting rate is higher. This higher unsteady available power level results in a lower SOC. At the higher TAC speed (lower thermal

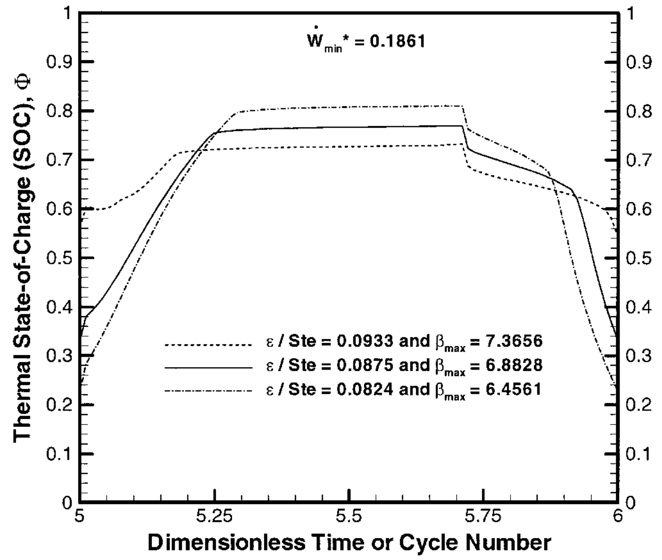

Fig. 11 Effect of thermal capacitance ratio on SOC over the balanced-orbit cycle.

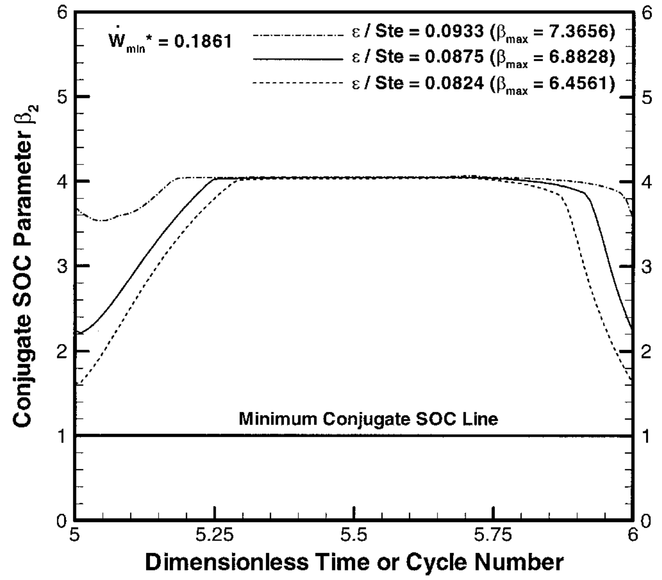

Fig. 12 Effect of thermal capacitance ratio on conjugate SOC parameter β_2 over the balanced-orbit cycle.

capacitance ratio), the PCM melting rate is lower, which results in a lower unsteady available power level and higher SOC. Once again, this phenomena is reversed during the eclipse period when all of the PCM superheat and latent heat has been removed. Furthermore, it is observed that some overlapping does occur during the eclipse period due to the different freeze rates associated with the different TAC speeds (thermal capacitance ratios). In quantitative terms, the sunrise SOC values corresponding to thermal capacitance ratios of 0.0933 (48,000-rpm TAC speed) and 0.0824 (56,000-rpm TAC speed) are approximately 57 and 24%, respectively; these are in contrast to the baseline SOC sunrise value of 33%. At sunset, these SOC values are approximately 80 and 72%, respectively, for thermal capacitance ratios of 0.0933 and 0.0824.

Figure 12 is a plot of the corresponding temporal variation of the second conjugate SOC function β_2 as a function of various thermal capacitance ratios (TAC speeds) over the balanced-orbit mode. Recall that the second conjugate SOC function β_2 is related to the instantaneous available power of the gas that is related to the receiver gas exit temperature [see Eq. (26)]. It is also weakly related to the pressure drop across each of the tubes in the receiver; typically, the outlet pressure is 2–3% lower than the inlet pressure,[8] which contributes negligibly to the loss in gas available power. In Fig. 12, some interesting phenomena can be observed. It is shown that the β_2 curve corresponding to the higher thermal capacitance ratio (lower TAC speed) of 0.0933 is higher than the other β_2 curves throughout the entire orbit period. During the initial sun period (approximately the first 5% of the total orbit period), the β_2 function for the higher thermal capacitance ratio (lower TAC speed) decreases; this is because during the initial sun period the thermal penetration waves have not propagated far enough into the PCM canisters to have a discernable effect on the receiver gas exit temperature. As a result, the receiver gas exit temperature and, hence, the β_2 function continue to decrease initially. This phenomenon is observed for only a minute fraction of the initial sun period for the baseline β_2 function and not at all for the β_2 function corresponding to the lower thermal capacitance ratio (higher TAC speed). Throughout most the latent regime (up to approximately 75% of the total orbit period), the β_2 function reaches a maximum value of about 4 for each of the thermal capacitance ratios. However, at sunrise, the β_2 function attains values of approximately 3.6 and 1.6, respectively, for thermal capacitance ratios of 0.0933 and 0.0824; the baseline sunrise value is approximately 2.2.

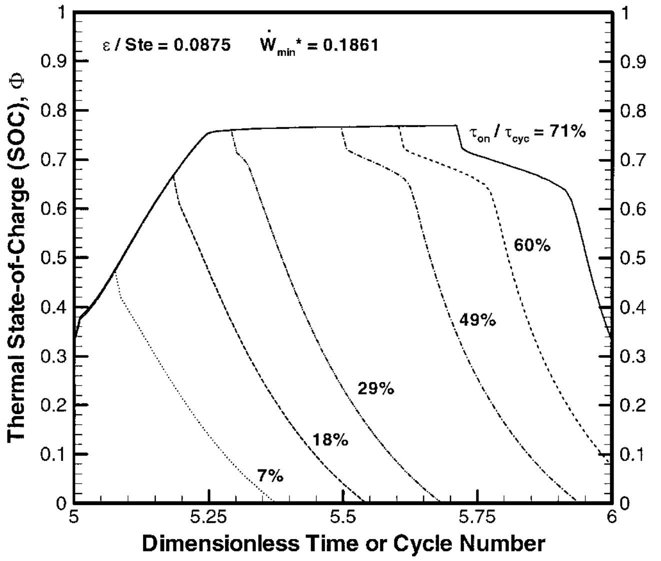

Fig. 13 Effect of sun period/total orbit period ratio on SOC over the balanced-orbit cycle.

The response of the primary SOC to changes in the sun period/total orbit period ratio is shown in Fig. 13. Comparisons are made for ratios ranging from the baseline value of 71% down to 7% over the balanced-orbit mode. The thermal capacitance ratio and dimensionless minimum gas available power are fixed at their baseline values of 0.0875 and 0.1861, respectively. This type of curve is important for two reasons: 1) For operation in the sun period, fault conditions such as concentrator off-pointing events can be characterized by pseudo-shutdown characteristic curves that eventually reach the zero SOC line. 2) During operation in the eclipse period, responses to orbital transfer events such as loss of altitude (or reboost to higher altitudes) can be characterized a priori to allow reassessment and/or adjustment of system operating parameters. Furthermore, these types of events aid the power management and distribution system in determining peak operating levels and safe operating margins. In Fig. 13, the baseline primary SOC curve is shown with a sun period/total orbit period ratio of approximately 71% (66 min. sun period and 93 min. total orbit period). As indicated in Fig. 13, as in Fig. 9, the sunrise value of the primary SOC is about 33%. It is also observed that the primary SOC curve corresponding to a sun period/total orbit period ratio of 60% is qualitatively similar to the baseline primary SOC curve. However, due to the longer eclipse period, the sunrise primary SOC value drops to approximately 8%. For the primary SOC curve corresponding to a sun period/total orbit period ratio of 49%, which is also qualitatively

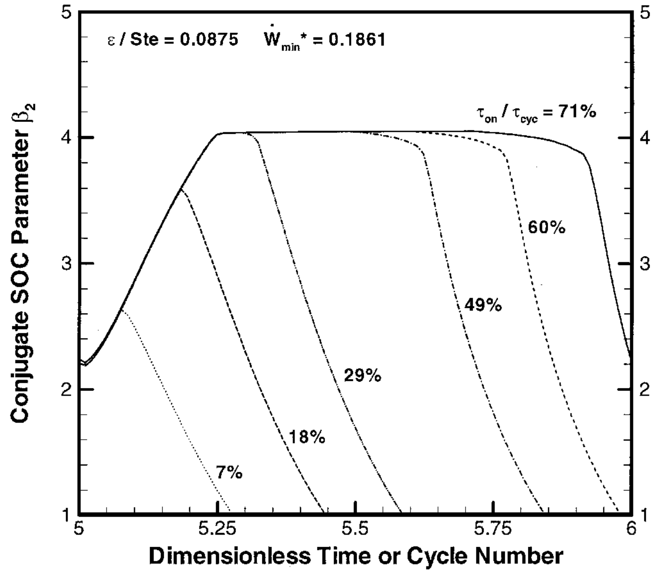

Fig. 14 Effect of sun period/total orbit period ratio on conjugate SOC parameter β_2 over the balanced-orbit cycle.

similar to the baseline primary SOC curve, the primary SOC reaches the zero SOC line prior to the end of the eclipse period. In fact, the system could only operate for approximately 93% of the baseline total orbit period, as indicated by where the curve crosses the zero SOC line. According to the primary SOC curve corresponding to a sun period/total orbit period ratio of 29%, which is qualitatively similar to the baseline primary SOC curve in the sensible regime, only about 67% of the baseline total orbit period can be used to operate the SD system. Moreover, for the primary SOC curves corresponding to sun period/total orbit period ratios of 18 and 7%, only about 54 and 37%, respectively, of the baseline total orbit period can be used.

Figure 14 shows the effect of parametric changes in the sun period/total orbit period ratio on the second conjugate SOC parameter β_2 during the balanced-orbit mode. Note the qualitative similarity between the baseline β_2 curve and the β_2 curves corresponding to reduced values of the sun period/total orbit period ratio. Also recall that the β_2 function is related to the dimensionless gas available power. In this regard, the β_2 function for all of the representative sun period/total orbit period ratios lag (in time) behind the corresponding primary SOC functions. As shown in Fig. 14, the β_2 curve corresponding to a sun period/total orbit period ratio of 60% reaches the minimum allowable value of unity before the end of the eclipse period. In fact, only about 97% of the baseline total orbit period can be used before operational changes have to be made. For a sun period/total orbit period ratio of 49%, the system can operate for only about 84% of the baseline total orbit period. This results in a 9% time lag behind the equivalent primary SOC function. When the sun period/total orbit period ratio is 29, 18, and 7%, the system can remain in operation for about 58, 44, and 27% of the baseline total orbit period, respectively; this corresponds to time lags of 9, 10, and 10%, respectively, behind the equivalent primary SOC values.

Conclusions

A theoretical framework for the determination of the thermal SOC of solar heat receivers employing encapsulated phase change storage has been developed, and results have been presented for the solar heat receiver component of NASA John H. Glenn Research Center at Lewis Field GTD System. The concepts of available power, virtual source temperature, and minimum gas available power have been used in the underlying theoretical analyses. Baseline conjugate and primary SOC curves were generated based on a priori known baseline system operating conditions through measurable parameters. Results indicated that for the baseline primary SOC curve in balanced-orbit mode, there was a 33% energy margin (from the minimum SOC line) at sunrise, which indicated safe operation of the solar dynamic system; at sunset, the primary SOC reached 76%. Furthermore, results for parametric changes indicated that the SOC in the sensible regimes was completely reversed in the latent regime. The second conjugate SOC curve was observed to lead the primary SOC curve (in time) with respect to operating the SD power system until their respective minimum SOC lines were reached.

Acknowledgments

The financial support of the NASA John H. Glenn Research Center at Lewis Field to Howard University under Grant NAG3-1907 is gratefully acknowledged. The partial support of the University of New Orleans is also acknowledged.

References

[1] Strumpf, H., Avanessian, V., and Ghafourian, R., "Design Analysis and Containment Canister Life Prediction for a Brayton Engine Solar Receiver for Space Station," *Journal of Solar Energy Engineering*, Vol. 116, No. 3, 1994, pp. 142–147.

[2] Jeffries, K. S. (ed.), *Solar Dynamic Power System Development for Space Station Freedom*, NASA Ref. Publ. 1310, July 1993.

[3] Bejan, A., *Entropy Generation Through Heat and Fluid Flow*, Wiley, New York, 1982, p. 32.

[4] Moynihan, P. I., "Second-Law Efficiency of Solar-Thermal Cavity Receivers," Jet Propulsion Lab. Publ. 83-97, California Inst. of Technology, Pasadena, CA, 1983.

[5] Hall, C. A., III, Glakpe, E. K., Cannon, J. N., and Kerslake, T. W., "Modeling Cyclic Phase Change and Energy Storage in Solar Heat Receivers," *Journal of Thermophysics and Heat Transfer*, Vol. 12, No. 3, 1998, pp. 406–413.

[6] Howell, J. R., *A Catalog of Radiation Configuration Factors*, McGraw–Hill, New York, 1982.

[7] Bellecci, C., and Conti, M., "Phase Change Energy Storage: Entropy Production, Irreversibility, and Second Law Efficiency," *Solar Energy*, Vol. 53, No. 2, 1994, pp. 163–170.

[8] Mason, L. S., "Solar Dynamic Power System Test Results," M.S. Thesis, Dept. of Mechanical Engineering, Cleveland State Univ., Cleveland, Ohio, May 1996.

[9] Shaltens, R. K., and Mason, L. S., "Early Results from Solar Dynamic Space Power System Testing," *Journal of Propulsion and Power*, Vol. 12, No. 5, 1996, pp. 852–858.

[10] Hall, C. A., III, "Thermal State-of-Charge of Solar Heat Receivers for Space Solar Dynamic Power," Ph.D. Dissertation, Dept. of Mechanical Engineering, Howard Univ., Washington, DC, May 1998.

[11] Shamsundar, N., and Sparrow, E. M., "Analysis of Multidimensional Conduction Phase Change via the Enthalpy Model," *Journal of Heat Transfer*, Vol. 97, No. 3, 1975, pp. 333–340.